

Trigger selenium sites and stable multiphasic-engineered modulated BiFeO₃/MoSe₂-1T/2H photocatalyst for hydrogen peroxide production

Kailin Xu ^{a,b}, Yueming Zhu ^c, Jin Qian ^{a,b,*}, Yuxuan He ^{a,b}, Yin Liu ^{a,b}, Bianhe Lu ^{a,b}, Sijing Tang ^{a,b}, Junwei Shen ^{a,b}

^a Key Laboratory of Integrated Regulation and Resource Development on Shallow Lakes, Ministry of Education, Hohai University, Nanjing 210098, People's Republic of China

^b College of Environment, Hohai University, Nanjing 210098, People's Republic of China

^c Nanjing Institute of Environmental Sciences, Ministry of Ecology and Environment, Nanjing 210042, People's Republic of China



ARTICLE INFO

Keywords:

Photocatalysis
Selenium sites
Stable multiphasic-engineered
H₂O₂ production

ABSTRACT

Regulating electron density at active sites holds profound importance in the advancement of highly efficient photocatalysts for hydrogen peroxide (H₂O₂) production. In this study, a novel and stable multiphasic BiFeO₃/MoSe₂-1T/2H (BFO/MSe) catalyst with selenium (Se) sites, was successfully synthesized. This catalyst exhibited distinctive multiphasic structures and an abundance of active sites, showcasing unexpectedly high activity and stability within photocatalytic systems. Notably, the optimized 4BFO/MSe demonstrated an outstanding catalytic rate for H₂O₂ production (1640 μmol·g⁻¹·h⁻¹). The spontaneously generated internal electric field facilitated charge transport, which enhanced the photocatalytic property. Moreover, the characteristics of multiphasic structures further facilitated efficient charge transfer and conduction, providing active sites. Furthermore, the electron-deficient Se sites (Se^{δ+}) within the BFO/MSe catalysts accelerated the redox cycling of transition metals, thereby accelerating the production of reactive oxygen species. By employing multiphasic engineering and Se sites, the potential applications of catalysts in H₂O₂ production can be effectively broadened.

1. Introduction

The contemporary global landscape is marked by pressing concerns centered around the energy crisis and environmental degradation [1]. Recently, there has been a noticeable surge in the interest directed towards hydrogen peroxide (H₂O₂) as an invaluable liquid solar fuel, due to its inherent transportability and storability attributes. Specifically, H₂O₂ is an environmentally benign oxidizer whose commercial value, impressive volumetric energy density has led to a wide range of applications in various industries such as paper and pulp production, wastewater treatment, disinfection, chemical synthesis, and fuel cell technology, etc [2,3]. Currently, the predominant industrial method for the synthesis of H₂O₂ involves the anthraquinone (AQ) oxidation process. Regrettably, this technique has significant limitations. It engendered considerable consumption of hydrogen (H₂) and fossil fuels, concurrently leading to the generation of substantial quantities of organic waste. Consequently, the exploration of alternative methodologies to engineer H₂O₂ synthesis with diminished energy outlay, waste

generation, production expenses, and safety concerns emerges as a compelling imperative [4]. Among the pursuit of viable solutions, photocatalytic technology emerged as a salient contender. Its efficacy in mitigating the dual challenges of energy scarcity and environmental exigency was underpinned by its cost-effectiveness, efficiency, and environmentally congenial character [5]. Notably, the field of photocatalysis has recently witnessed considerable research attention channeled towards the photocatalytic generation of H₂O₂ using semiconductors, facilitated by the oxygen reduction reaction (ORR). The process is based solely on light, water and oxygen as elemental precursors. This underscores its inherent environmental sustainability.

Recently, ferroelectric semiconductors of the perovskite-type ABO₃, with BiFeO₃ (BFO) as a notable exemplar, have attracted attention in the field of photocatalysis. The elevated attention toward these ferroelectric semiconductors, exceeding that devoted to traditional metallic compound photocatalysts, can be ascribed to their exceptional light absorption capabilities. Additionally, their distinctive feature of adjustable spontaneous polarization exerts a significant influence over charge

* Corresponding author at: Key Laboratory of Integrated Regulation and Resource Development on Shallow Lakes, Ministry of Education, Hohai University, Nanjing 210098, People's Republic of China.

E-mail address: hhuqj@hhu.edu.cn (J. Qian).

dynamics [6]. The intrinsic characteristic of spontaneous polarization found in ferroelectric materials has proven to be highly effective in driving efficient charge separation [7,8]. For example, Li et al. emphasized the significant enhancement of photocatalytic performance for the H₂ evolution of PbTiO₃ material [9]. Despite the intriguing interplay between spontaneous polarization and carrier properties, particulate BFO as a representative ferroelectric material commonly exhibits lack-luster photocurrent and suboptimal catalytic activity [10]. In addition, the inherent complexity of crystal phase changes, defect concentration and domain wall distribution in particulate BFO also poses a challenge for photocatalytic applications [11–13].

To overcome the above limitations, a widely adopted approach has been the integration of photocatalysts with cocatalysts. This strategy serves a dual purpose: first, to enhance charge separation and transport processes; and second, to provide active sites that accelerate interfacial catalytic reactions [14,15]. Among the range of cocatalyst systems, two-dimensional transition metal selenides (TMS) have received particular attention in the field of photocatalysis due to their cost effectiveness, natural abundance, and enormous specific surface area [16,17]. It is noteworthy that the prevailing focus concerning well-researched 2D TMSs pertains to the semiconductor phase (2 H) (e.g., 2 H MoSe₂, 2 H CoSe₂), primarily due to their straightforward synthesis protocols and robust structural stability [18]. Surprisingly, research has showed that introducing multiphase 1 T/2 H MoSe₂, which entails introducing the 2 H phase into the 1 T phase MoSe₂ structure, resulted in increased catalytic activity. This phenomenon is due to the increased abundance of active basal planes and improved conductivity inherent in the asymmetric configuration of the material [19,20]. For example, Wang et al. showcased the superior photodegradation capabilities of 1 T/2 H MoSe₂/pg-C₃N₄ in contrast to pure 2 H MoSe₂/pg-C₃N₄ composites [21]. Therefore, the development of highly efficient 1 T/2 H MoSe₂ is a promising way to attain enhanced performance in photocatalytic H₂O₂ production. Unfortunately, 1 T/2 H MoSe₂ structures often exhibit relatively weak selenium-oxygen (Se-O_{ads}) bonds, attributed to their less-than-ideal electronic configuration [22,23], as depicted in Fig. S1. Consequently, the intricate architecture of these materials introduces significant challenges in precisely regulating the strength of Se-O_{ads} bonds at the in-plane Se sites. This regulation is critical for evaluating interfacial catalytic efficiency and elucidating nuanced configuration-activity relationships. Hence, there exists a compelling need to explore effective modification strategies aimed at enhancing the strength of Se-O_{ads} bonds. This improvement has been critical to achieving higher levels of efficiency in photocatalytic H₂O₂ production.

Interestingly, recent reports have indicated that the enriched metal-metal bonds observed in TMSs are associated with the presence of distinct localized electrons, attributed to the robust binding affinity within these bonds. These localized electrons act as a reservoir, effectively modulating the electronic configuration of adjacent atoms [24]. Exploiting this premise, it was anticipated that precise manipulation of the local microenvironment within the BiFeO₃/MoSe₂-1 T/2 H (BFO/MSe) catalyst could be used to optimize the binding strength of Se-O_{ads} at in-plane Se sites. This strategic optimization has the potential to significantly enhance the efficiency of interfacial H₂O₂ production [25]. In this work, the newly identified oxygen-metal configuration (Fe-O-Mo) plays a pivotal role. This configuration orchestrates the attenuation of the electron distribution in the proximity of in-plane Se sites, thus inducing the directional activation of specific Se sites within the BFO/MSe catalyst. This activation mechanism notably enhances the catalytic efficiency of H₂O₂ production.

2. Experimental

2.1. Regents and characterization

Regents and characterization methods were displayed in Text S1.

2.2. Preparation of BFO material

First, 3.88 g of Bi(NO₃)₃•5 H₂O and 3.23 g of Fe(NO₃)₃•9 H₂O were dissolved in 20 mL of 2 M HNO₃ and glycol (volume ratio of nitric acid/glycol was 1:1) and then stirred in a constant temperature water bath at 80 °C for 12 h. The resulting mixture was calcined at 500 °C for 2 h. The obtained brown powder was washed alternately with ethanol and water three times and dried at 80 °C for 12 h to obtain BFO catalyst.

2.3. Fabrication of BFO/MSe composites

First, 1 mmol of Na₂MoO₄•2 H₂O was added to 30 mL of distilled water and stirred for 20 min at room temperature to form A solution. Then, 2 mmol of Se powder was mixed with 10 mL of hydrazine hydrate (N₂H₄•H₂O) and placed under a magnetic stirrer at 25 °C for 20 min to form B solution. Subsequently, the mixture was obtained by adding solution B to solution A. Certain BFO material was added to the above mixture and ultrasonic measurements were performed for 20 min. BFO was injected in the amounts of 0.3 g, 0.4 g, and 0.5 g, respectively. Afterward, the above solution was transferred to a 100 mL Teflon-lined autoclave and heated at 220 °C for 24 h. The obtained sediment was washed with deionized water and dried at 80 °C for 12 h, and named xBFO/MSe composite (x = 3, 4, 5).

2.4. Photocatalytic H₂O₂ production

50 mg of the photocatalyst was dispersed in 95 mL of deionized water and 5 mL of ethylene glycol (EG). Then, the pollutant solution was injected with oxygen (O₂) in the dark condition at 25 °C for 30 min to reach O₂ dissolution saturation. Subsequently, the xenon lamp (300 W) equipped with a 420 nm cut-off filter was used to provide the light source. During the reaction, O₂ was continuously supplied and the reaction temperature was maintained at 25 °C with the use of condensate. After the reaction, 1 mL aliquot was extracted from the suspension and the photocatalyst was filtered through a 0.22 μm cellulose membrane. All photocatalytic experiments were performed three times at room temperature under optimum conditions.

2.5. Electrochemical measurements

Electrochemical measurements were shown in Text S2.

2.6. DFT calculation

DFT calculations were shown in Text S3.

3. Results and discussion

3.1. Morphology analysis

The morphology of BFO, 1 T/2 H MoSe₂, and BFO/MSe samples could be characterized by SEM analysis. As depicted in Fig. 1a, the SEM image of pristine BFO exhibited irregular polyhedral morphology with irregular shapes and uniform size distribution, consistent with previous reports [26]. Fig. 1b displayed 1 T/2 H MoSe₂ composed of small particles with sizes ranging approximately from 70 to 90 nm. Moreover, the 1 T/2 H MoSe₂ exhibited a nanoflower-like morphology composed of nanosheets. Fig. 1c and d demonstrated the modification of 1 T/2 H MoSe₂ nanosheets on the polyhedral surface of BFO, thereby confirming the successful fabrication of the BFO/MSe composite. Moreover, the HRTEM image depicted in Fig. 1e revealed that the nanosheet exhibited a specific plane spacing of 0.284 nm, precisely corresponding to the (100) plane of 1 T/2 H MoSe₂. Additionally, a lattice spacing of 0.278 nm was discerned, attributed to BFO, aligning with the (110) hexagonal pattern. Notably, a well-defined and compact interface emerged between BFO and 1 T/2 H MoSe₂, facilitating efficient electron transfer.

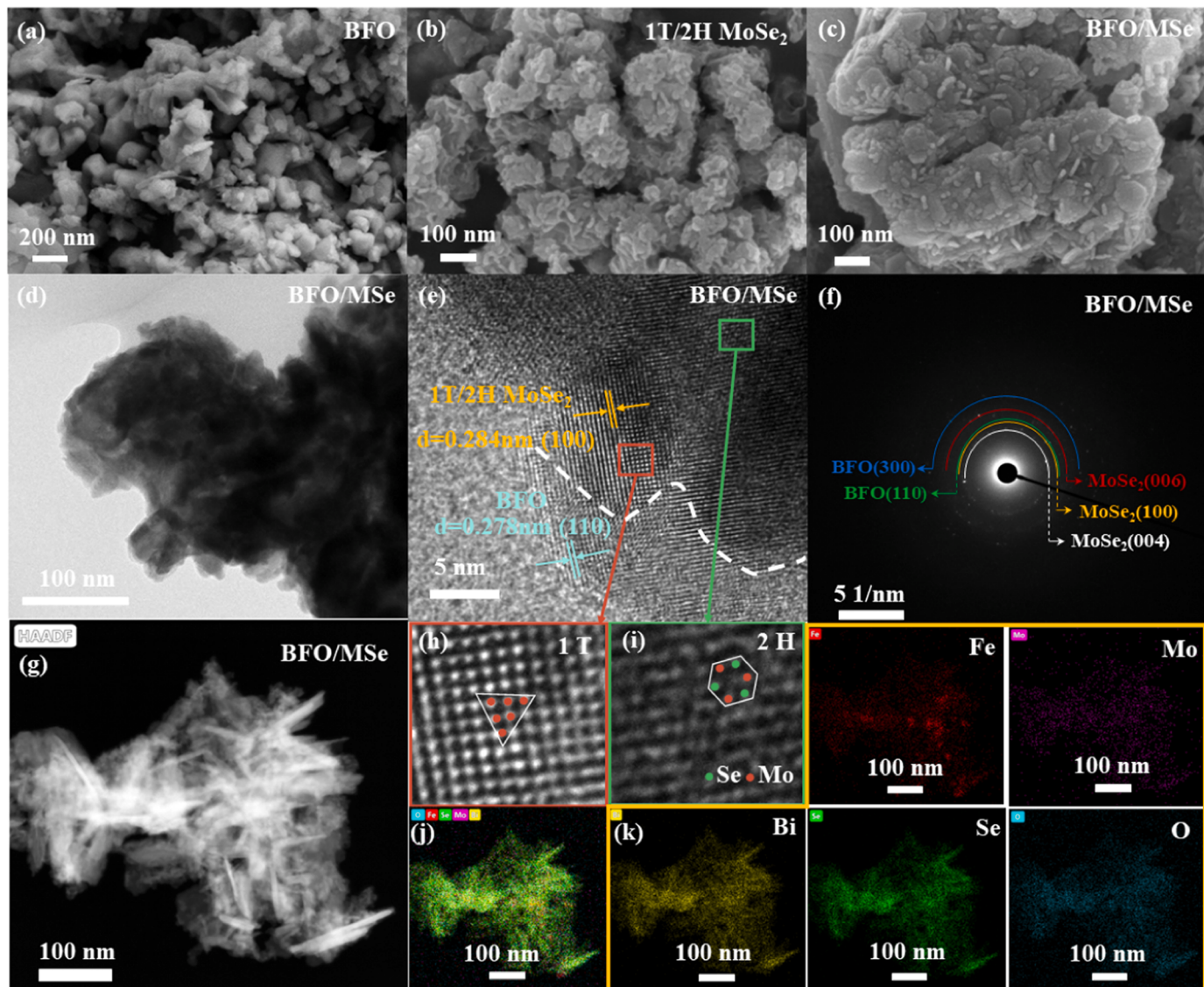


Fig. 1. SEM images of (a) BFO, (b) 1 T/2 H MoSe₂ and (c) BFO/MSe, (d) TEM images of BFO/MSe, (e) HRTEM images of BFO/MSe, (f) SAED pattern of BFO/MSe, (g, j, k) Mapping of BFO/MSe, (h, i) HRTEM images of BFO/MSe with 1 T and 2 H MoSe₂ phases.

Importantly, the magnified HRTEM images in Fig. 1h and i revealed triangular lattice regions and honeycomb lattice regions, serving as clear indicators of the coexistence of 1 T and 2 H phases within BFO/MSe composite, thereby substantiating the presence of both structural phases. The incorporation of the 2 H phase in the BFO/MSe composite resulted in a visible-light bandgap, semiconductor behavior, and metallic attributes due to the high conductivity of the 1 T phase, leading to enhanced photocatalytic performance. Furthermore, as shown in Fig. 1f, the SAED pattern of the synthesized BFO/MSe nanocomposite displayed concentric rings of diffraction spots, corresponding to various crystallographic planes observed in the XRD pattern, thereby confirming the polycrystalline nature of BFO/MSe composite. In addition, two SAED diffraction patterns were collected within the BFO/MSe composite of Fig. S2. Taking into account systematic errors in SAED experiments and standard instrument imperfections into account, both collected diffraction patterns could be identified as belonging to the 1 T and 2 H phases. This was also consistent with the HRTEM results. To investigate the elemental dispersion in the BFO/MSe composite, the Energy Dispersive Spectrometer (EDS) mapping was performed in Fig. S3. As depicted in Fig. 1g, j, k, a uniform distribution of Bi, Fe, Mo, O, and Se elements was observed, confirming the uniform contact between BFO and 1 T/2 H

MoSe₂ as well as the uniform growth of 1 T/2 H MoSe₂ on the BFO material.

3.2. Composition analysis

The XRD patterns of BFO, 1 T/2 H MoSe₂ and BFO/MSe material were presented in Fig. 2a. In the case of BFO (JCPDS No. 20-0169), the peaks located at 22.49°, 31.81°, 32.14°, 39.51°, 45.81°, 51.38°, and 57.01° were found to precisely match the crystal planes (012), (104), (110), (202), (024), (116), and (214) respectively [27]. Similarly, for 2 H MoSe₂ (Fig. S4), the major peaks were detected at 13.62°, 31.60°, 37.96°, 47.49°, and 56.66°, which corresponded to the crystal planes (002), (100), (103), (105), and (110), respectively, based on JCPDS No. 29-0914 [28]. The (002) peak of 1 T/2 H MoSe₂ was slightly shifted and the peak intensity decreased as compared to that of 2 H MoSe₂. The above changes in the XRD results are consistent with those reported for the transition from the 2 H phase to the 1 T phase of MoSe₂ [29]. The XRD of 1 T/2 H MoSe₂ exhibited a broad envelope shape, which is caused by the low crystallinity and the presence of dual phase 1 T/2 H MoSe₂ [30]. The diffraction peak observed at 13.6° in 1 T/2 H MoSe₂ provided evidence for its layered crystalline structure, which was

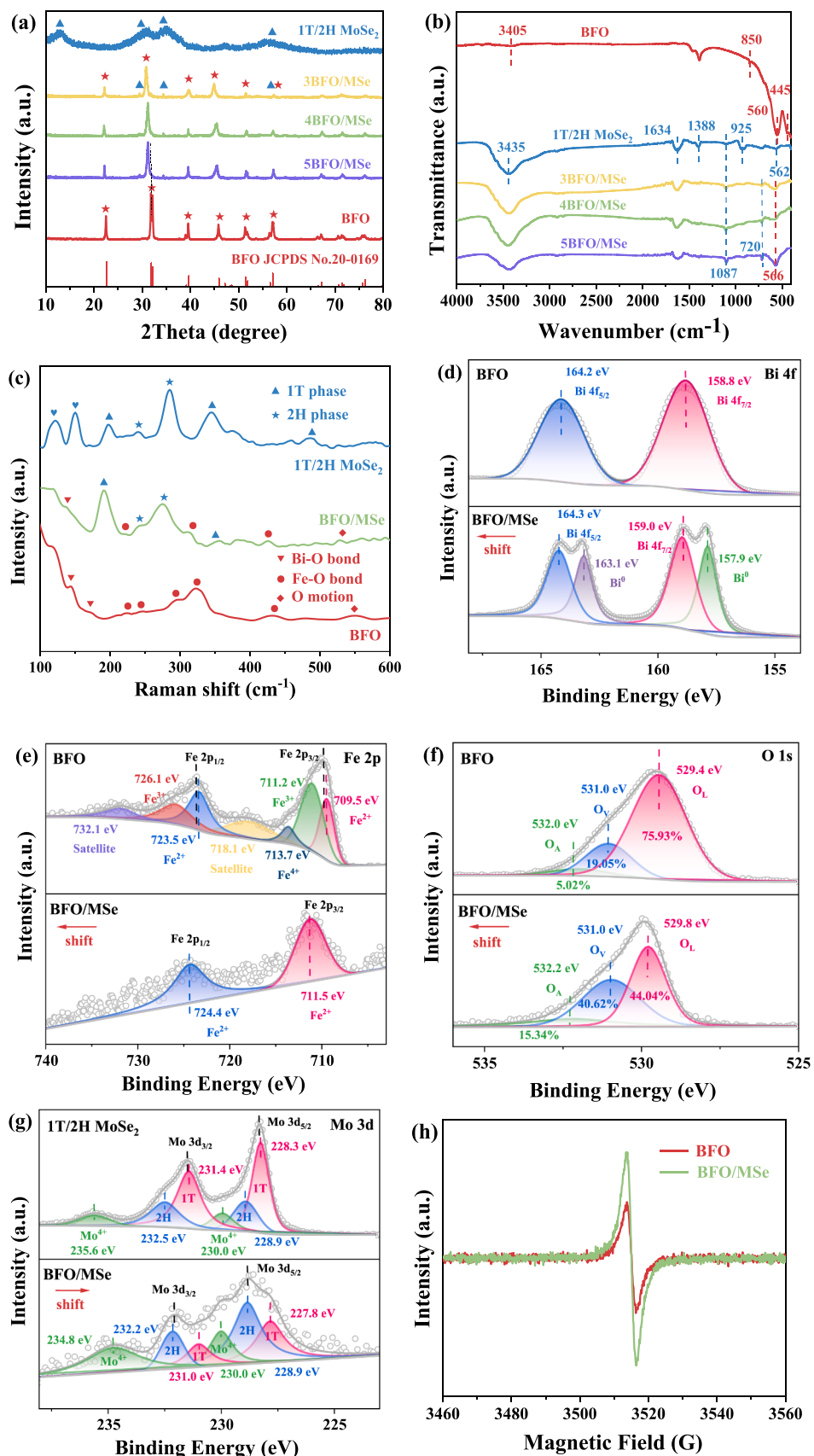


Fig. 2. (a) XRD diffraction spectrum, (b) FT-IR spectra, (c) Raman spectrum of BFO, 1 T/2 H MoSe₂, and BFO/MSe; (d) Bi 4 f XPS spectra, (e) Fe 2p XPS spectra, (f) O 1 s XPS spectra of BFO and BFO/MSe; (g) Mo 3d XPS spectra of 1 T/2 H MoSe₂ and BFO/MSe; (h) EPR of BFO and BFO/MSe.

characterized by weak Van der Waals interactions between Se-Mo-Se layers [31]. Compared to BFO, the BFO/MSe samples exhibited a shift of all diffraction peaks towards lower angles due to the apparent interface interaction caused by 1 T/2 H MoSe₂.

This interaction was further investigated by FT-IR measurements. In Fig. 2b of BFO, the peak at 3405 cm⁻¹ was attributed to adsorbed water from the atmosphere. The fundamental absorption band of BFO was found in the range of 445–560 cm⁻¹, corresponding to the bending and stretching vibrations of Fe-O and Bi-O bonds [32]. Additionally, an absorption band at 850 cm⁻¹ originated from the symmetric stretching vibration of O-Bi-O in the BiO₃ unit, indicating the formation of BFO [33]. Furthermore, peaks corresponding to 1 T/2 H MoSe₂ were observed at 1087, 1388, and 1634 cm⁻¹, which corresponded to the deformation of Se-O bonds, C=O, and COO- stretching vibrations [34]. Peaks related to Se-Se and Se-O-Se were also observed at 562 and 925 cm⁻¹, respectively [35]. Various absorption peaks corresponding to Mo-OH were detected at 3435 cm⁻¹ [36]. It was noteworthy that the Mo-O content at 720 cm⁻¹ increased with the addition of BFO, suggesting a possible bond formation between the O element in BFO and the Mo element in 1 T/2 H MoSe₂. In addition, the presence of Mo-O and Se-O bonds in BFO/MSe demonstrated that the catalytic activity of the catalyst was significantly improved due to the strong electrical interaction generated by the oxygen substitution sites [37]. Besides, slight shifts were observed in the Bi-O and Fe-O spectral bands from 560 to 566 cm⁻¹, indicating the influence of 1 T/2 H MoSe₂ on the structural strength of the vibrational units in BFO, which was consistent with the XRD results.

The Raman spectrum in Fig. 2c displayed characteristic peaks of BFO, 1 T/2 H MoSe₂, and BFO/MSe composite. In 1 T/2 H MoSe₂, strong peaks were observed at 238.8 and 285.1 cm⁻¹, corresponding to the in-plane A_{1g} and out-of-plane E_{2g}¹E_{2g}¹ modes of the 2 H phase, respectively. Peaks attributed to the J₁, J₂, and J₃ modes of the 1 T phase appeared at 196.4, 346.8, and 487.5 cm⁻¹, respectively [38]. Additional modes also appear at 116.3 and 150.1 cm⁻¹. These modes result from the reduction of the in-plane symmetry from D_{3h} in the trigonal planar coordination of Mo in 2 H phase to a lower in-plane symmetry in the 1 T phase, which has a distorted octahedral coordination of the Mo atoms [39]. In the context of BFO, the low-frequency phonon modes observed around 144 and 173 cm⁻¹ primarily represented the A1 mode associated with the vibration of Bi-O bonds. Shifting to 221 and 244 cm⁻¹ was attributed to the vibrations of Fe-O bonds within the FeO₄ tetrahedra. Phonon modes originating from Fe-O vibrations within FeO₆ octahedra were identified at 290, 323, and 429 cm⁻¹. Additionally, the phonon mode at 549 cm⁻¹ corresponded to the atomic vibration of O motion within the FeO₆ octahedra [40]. In comparison to both BFO and 1 T/2 H MoSe₂, the Raman modes in the heterojunction of BFO/MSe composite exhibited a shift towards lower wavenumbers, signifying an increased asymmetry of the FeO₄ tetrahedra and FeO₆ octahedra units due to the displacement of the center of gravity away from the Fe ion. This structural alteration suggested the establishment of charge transfer channels between BFO and 1 T/2 H MoSe₂. Furthermore, the O atoms within the FeO₆ units also underwent Raman shifts in BFO/MSe composite. The resulting unequal Mulliken charges on the O atoms may augment the interfacial internal electric fields (IEF) due to the generated dipole moment, consequently enhancing effective carrier separation and transfer.

The findings were substantiated through comprehensive XPS analysis. The entirety of the Bi, Fe, O, Mo, and Se constituents within the BFO/MSe composite structure were discerned from the comprehensive XPS full-scan spectrum (Fig. S5a). Additionally, the elemental composition of the BFO/MSe composite, as detailed in Table S1, harmonized with the outcomes of elemental mapping analyses. In Fig. 2d, the distinctive division of Bi 4 f peaks at 158.8 and 164.2 eV corresponds respectively to Bi 4 f_{7/2} and Bi 4 f_{5/2}, attesting to the presence of Bi³⁺ species within the BFO material [41]. On the contrary, the distinct peaks observed at 157.9 and 163.1 eV, associated with Bi⁰ species [42], were

conspicuously present only in the BFO/MSe composite. This change suggested that Bi atoms tended to function as electron acceptors. The discernible Fe 2p peaks (Fig. 2e) appeared at binding energies of 711.5 and 724.4 eV, corresponding to Fe 2p^{3/2} and Fe 2p^{1/2}, respectively. In contrast, the Fe 2p peaks in pure BFO exhibited binding energies of 709.5 and 723.5 eV, denoting Fe²⁺, along with the peak at 711.2 and 726.1 eV indicating Fe³⁺ [43]. Furthermore, the peak at 713.7 eV was attributed to Fe⁴⁺ [44]. Notably, the introduction of 1 T/2 H MoSe₂ was found to influence the valence states of the Fe species. From the O 1 s high-resolution spectrum (Fig. 2f), the deconvolution of peaks at 529.4, 531.0, and 532.0 eV assigned these to lattice oxygen (O_L), surface oxygen vacancies (O_V), and oxygen species absorbed at hydroxyl and water sites (O_A), respectively [45]. The discernible abundance of O_V within the BFO/MSe composite (with O_V accounting for 40.62 % of the cumulative oxygen content) offers numerous exciton capture sites at the heterojunction interface [46]. The prevalence of these vacancies stems from transitions such as Fe³⁺/Fe⁴⁺ to Fe²⁺ and Bi³⁺ to Bi⁰ within the BFO/MSe composite. Moreover, the XPS spectra validated the presence of distinct phase structures within 1 T/2 H MoSe₂. In the high-resolution Mo 3d spectrum, the peaks observed at 228.3 and 231.4 eV corresponded to the 1 T phase, while those at 228.9 and 232.5 eV indicated the 2 H phase. Additionally, Mo⁴⁺ peaks were observed at 230.0 and 235.6 eV, as shown in Fig. 2g [47]. The Se 3d spectrum further corroborated this mixed phase configuration (Fig. S5b), displaying four peaks at 53.7 and 54.8 eV for the 1 T phase and 54.2 and 55.6 eV for the 2 H phase. The shift indicated the presence of Se^{δ+} in BFO/MSe. These findings align primarily with the Mo 3d spectroscopic and Raman analysis, underscoring the prevalence of the 1 T phase [12]. However, within the BFO/MSe heterojunction, an increased presence of the 2 H phase was evident due to the thermodynamically driven metastable-to-stable transition of the 1 T phase MoSe₂ [48]. Regarding the BFO/MSe heterojunction, discernible shifts towards higher binding energies were noted in the Bi 4 f, Fe 2p, and O 1 s peaks. Conversely, the Mo 3d and Se 3d peaks exhibited downward shifts compared to those of 1 T/2 H MoSe₂. These shifts in binding energies were ascribed to electron transference from BFO to 1 T/2 H MoSe₂, facilitated by Van der Waals interactions at their interfacial region. This interaction effectively augmented the separation and conveyance of photoinduced charge carriers [49,50], corroborating with the findings from XRD and FT-IR results.

This O_V was further detected in the XPS analysis by EPR measurements. As illustrated in Fig. 2h, symmetric EPR signal peaks were discerned at g = 2.004 for both the BFO and BFO/MSe samples, with the peak intensity being most pronounced in the BFO/MSe composite. This observation unequivocally substantiates the existence of O_V in both the BFO and BFO/MSe material, and it also underscored an elevated concentration of O_V after the introduction of 1 T/2 H MoSe₂ dopants. Additionally, the XPS analysis revealed a pertinent detail concerning the origin of these O_V in BFO/MSe composite, establishing that they predominantly stem from the BFO material. This was because when 1 T/2 H MoSe₂ catalyst combines with BFO, Fe-O-Mo bonds were formed to carry away oxygen species, while generating O_V, forming a Fe-O_V-Mo interface. According to the peak shifts of XPS and Raman analysis, a charge transfer channel had been established between BFO and 1 T/2 H MoSe₂, which may be due to the role of the Fe-O-Mo bonds.

3.3. Photocatalytic properties

The photocatalytic experiments were initially conducted by suspending the samples in O₂-saturated pure water under visible-light irradiation. The average rates of H₂O₂ production for the BFO, 1 T/2 H MoSe₂, 3BFO/MSe, 4BFO/MSe, and 5BFO/MSe samples were determined to be 10, 24, 55, 82, and 61 μmol•h⁻¹, respectively (Fig. 3a). It was noteworthy that the 4BFO/MSe composite exhibited the highest photocatalytic H₂O₂ yield, reaching 1640 μmol•g⁻¹•h⁻¹. This observation underscored a significant enhancement in the photocatalytic

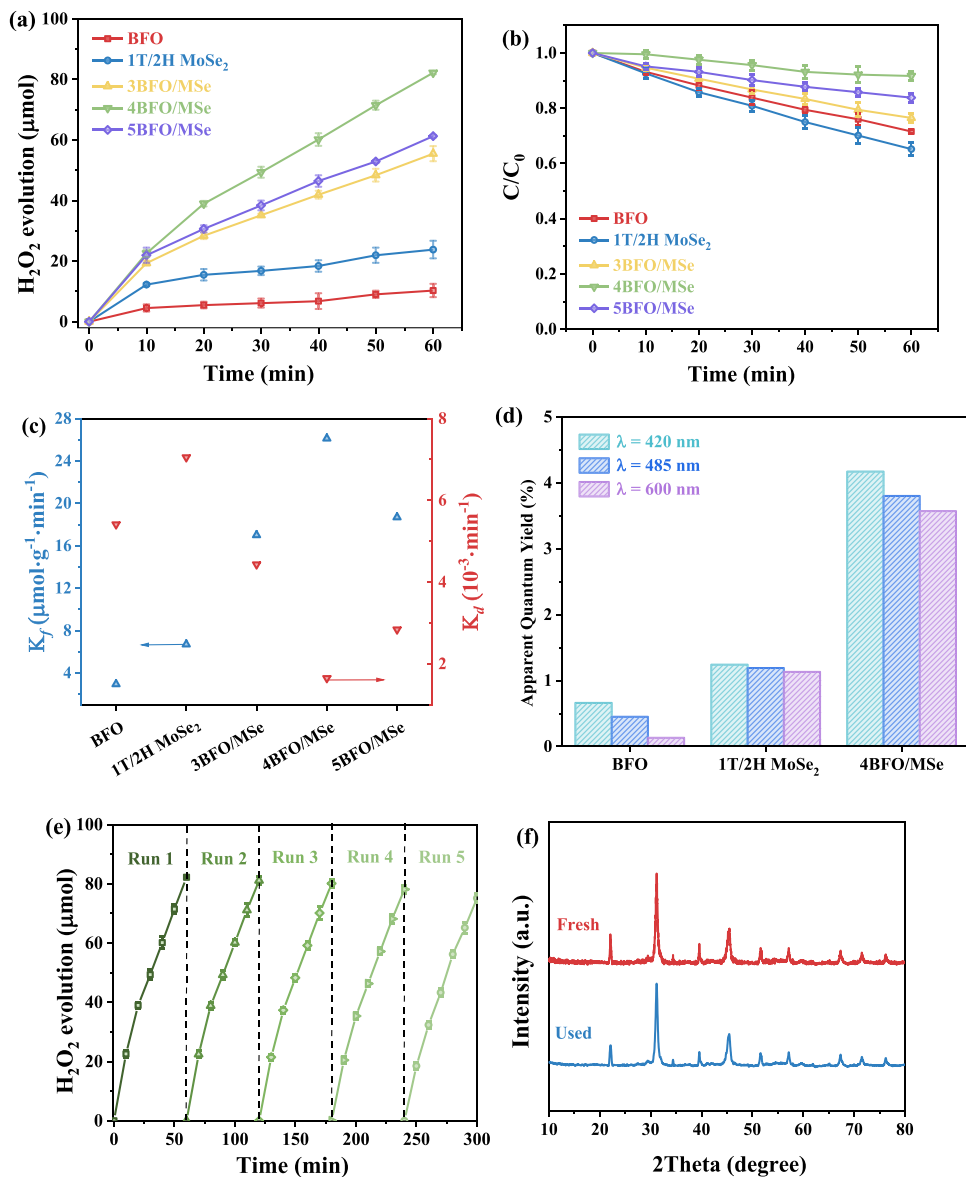


Fig. 3. (a) Photocatalytic generation of H_2O_2 over as-prepared samples under light irradiation; (b) Photocatalytic decomposition of $1 \text{ mmol}\cdot\text{L}^{-1}$ H_2O_2 over as-prepared samples; (c) The formation rate constants (K_f) and decomposition rate constants (K_d) of H_2O_2 for as-prepared samples; (d) Apparent quantum yield at different wavelengths; (e) Cyclic tests of 4BFO/MSe for H_2O_2 production; (f) XRD survey for fresh and used for 4BFO/MSe.

performance for H_2O_2 production achieved by the 4BFO/MSe composite when compared to both the BFO and 1 T/2 H MoSe₂ material. This outcome substantiated the synergistic effect arising from the combination of BFO and 1 T/2 H MoSe₂ in enhancing photocatalytic H_2O_2 production. The addition of an appropriate amount of BFO can reduce the transfer distance of photo generated charge carriers, thereby providing more active sites for photocatalytic reactions. However, excessive addition of BFO can enhance the decomposition of H_2O_2 and reduce the photocatalytic performance of the material. Additionally, as depicted in Fig. S6, the photocatalytic performance of the 4BFO/MSe-2 H material demonstrated a much lower H_2O_2 generation rate in contrast to the 4BFO/MSe-1 T/2 H photocatalysts. The synthesis method of the 4BFO/MSe-2 H material was shown in Text. S4. This difference was due to the fact that 1 T/2 H MoSe₂ had more active edge sites and better conductivity compared to 2 H MoSe₂ material. H_2O_2 was produced and broken down via photocatalysis, which represented two opposing routes. To explore the breakdown behavior of H_2O_2 , photocatalytic decomposition tests were performed with all materials at an initial H_2O_2 concentration of $1 \text{ mmol}\cdot\text{L}^{-1}$ in the absence of O_2 . The results of these tests were given

in Fig. 3b. In contrast to the other materials, the 4BFO/MSe catalyst exhibited a substantially lower H_2O_2 decomposition rate (8.3 %) after 1 h. It was important to emphasize that the production and decomposition of H_2O_2 may both be explained by first- and zero-order kinetics [51,52]. Therefore, the rate constants for H_2O_2 formation (K_f , $\mu\text{mol}\cdot\text{g}^{-1}\cdot\text{min}^{-1}$) and decomposition (K_d , min^{-1}) rate were separately determined [53]. Fig. 3c compared the K_f and K_d values of all samples. Bare BFO and 1 T/2 H MoSe₂ exhibited relatively higher K_d and lower K_f , leading to the mediocre production of H_2O_2 . The incorporation of BFO into 1 T/2 H MoSe₂ increases K_f and decreases K_d values. Notably, the 4BFO/MSe catalyst showed the highest K_f and the lowest K_d , which contributed to the best H_2O_2 production performance. This could be ascribed to the improved electron-hole separation in the BFO/MSe hybrid. According to Fig. 3d and the calculation process of Table S2 [54–56], 4BFO/MSe catalyst displayed much higher apparent quantum yields (AQY) than BFO and 1 T/2 H MoSe₂ at various wavelengths. The results indicated that effective utilization of incident light was beneficial for improving the photocatalytic activity of 4BFO/MSe material.

The photocatalytic H_2O_2 generation experiment was performed five

times to further examine the recyclable nature of the 4BFO/MSe catalyst (Fig. 3e). Five cycles after compounding, the photodegradation efficiency of 4BFO/MSe catalyst exhibited a small decline, showing that 4BFO/MSe catalyst had strong reusability for producing H₂O₂. As shown in Fig. 3f and Fig. S7, the recycled 4BFO/MSe catalyst showed high stability in the XRD and FT-IR. Furthermore, the photocatalytic efficiency of the BFO/MSe catalyst was compared to the literature, with the findings shown in Table S3. BFO/MSe catalyst had a greater photocatalytic H₂O₂ performance than most published values, suggesting its promise in photocatalytic H₂O₂ generation.

3.4. Optical and electrochemical performance

UV-vis DRS was utilized to explore the optical bandgap and photo-absorption characteristics of BFO, 1 T/2 H MoSe₂, and BFO/MSe composites, as depicted in Fig. 4a. Pure BFO exhibited a distinct photo-absorption edge at 570 nm, denoting a sharp transition. The

pronounced absorption edges observed in perovskite-type oxide materials are primarily attributed to electronic transitions from the O 2p valence band (VB) to the Fe 3d conduction band (CB) [11]. In comparison, the absorption edge of the BFO/MSe composite displayed a redshift in comparison to pure BFO, indicating that the incorporation of 1 T/2 H MoSe₂ could enhance light absorption in the composite due to its strong light-harvesting capabilities. Furthermore, the BFO/MSe composites may greatly increase the intensity of full-light absorption. Simultaneously, the BFO band structures were determined by estimating the straight line to X-axis intercept from the plot of $(\alpha h\nu)^{1/2}$ versus $h\nu$ [57]. The E_g of 2.14 eV for BFO (direct semiconductor, n = 1/2) was shown in Fig. 4b.

The XPS regression line (Fig. 4c) was extended until it intersected the flat section of the curve at the predicted VB potentials of BFO and 1 T/2 H MoSe₂ material, which were measured at 1.83 and 0.98 eV, respectively. To ascertain the conductivity type and flat band potential (E_{fb}) of semiconductors, a tangent was drawn along the longest line of

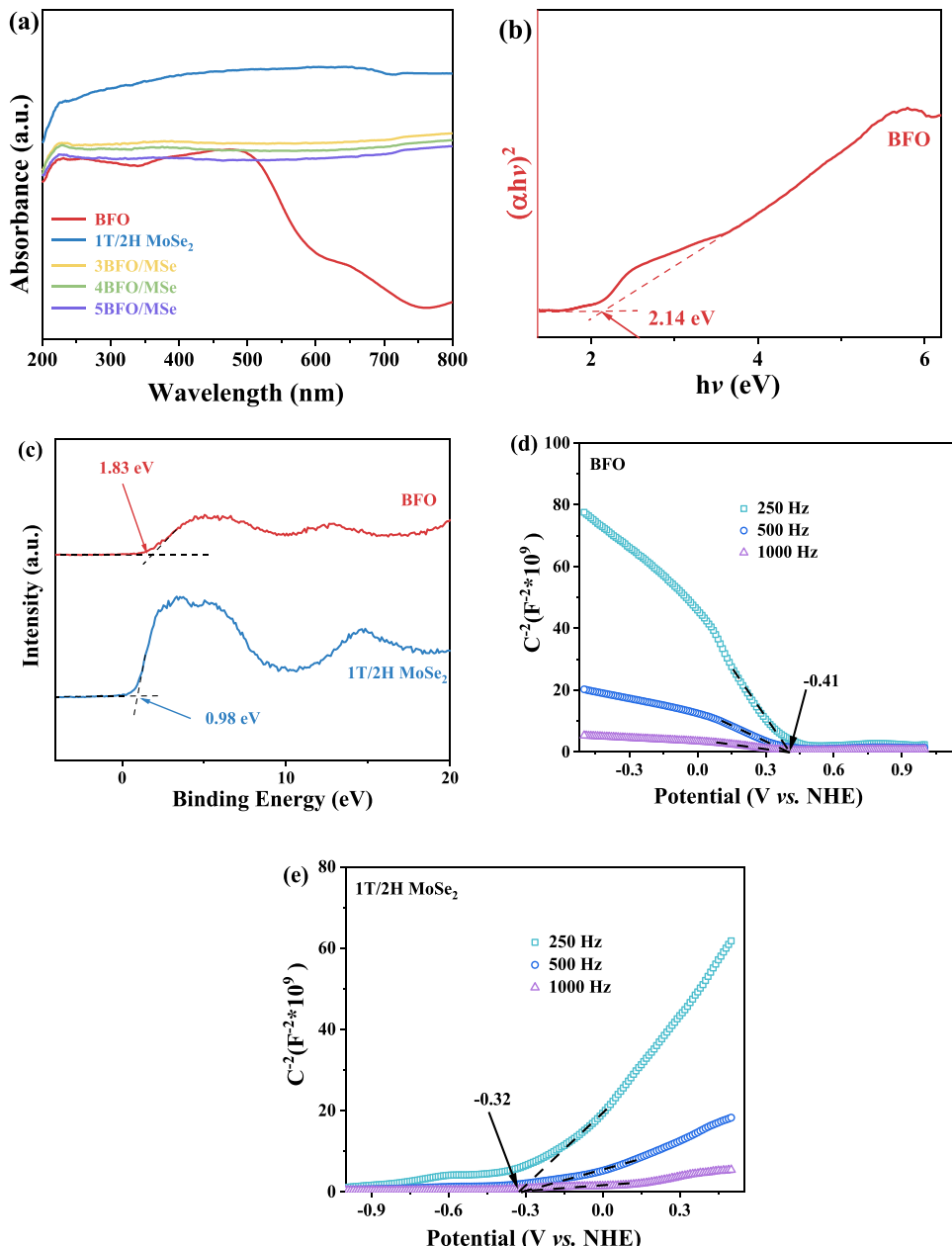


Fig. 4. (a) UV-vis DRS spectra of the BFO, 1 T/2 H MoSe₂, and BFO/MSe; (b) The estimated band gap curves of the BFO and 1 T/2 H MoSe₂; (c) Total densities states of XPS valence band for the BFO and 1 T/2 H MoSe₂; Mott-Schottky plots of (d) BFO and (e) 1 T/2 H MoSe₂.

the Mott-Schottky curve. A positive slope indicated an n-type semiconductor, while a negative slope denoted a p-type semiconductor, both constituting conductive semiconductor types. As shown in Fig. 4d and e, BFO exhibited characteristics of a p-type semiconductor, whereas 1 T/2 H MoSe₂ exhibited characteristics of an n-type semiconductor [58]. Furthermore, the flat band potentials for BFO and 1 T/2 H MoSe₂ were determined to be -0.41 and -0.32 V, respectively. Additionally, the equation $E_g = E_{VB} + E_{CB}$, where E_{VB} represented the VB potential and E_{CB} represented the CB potential, was employed to ascertain key elements of the electronic band structure. For BFO, the E_{CB} calculation values were -0.31 eV. This was consistent with the typical positioning of the CB of p-type semiconductors on the Mott-Schottky curve, usually being $0.1\text{--}0.2$ V higher than their flat band potential [59]. In addition, according to the CB of n-type semiconductors, their flat band potential was usually $0.1\text{--}0.2$ V lower than the CB. The E_{CB} of MoSe₂ was about -0.47 eV. Therefore, the E_g of 1 T/2 H MoSe₂ can be determined to be 1.45 eV. In addition, according to Fig. S8, the VB, CB and E_g of 2 H MoSe₂ are 1.37 , -0.35 and 1.72 eV, respectively.

To investigate the causes for the considerable enhancement in

photocatalytic activity, the transient photocurrent response and EIS under visible light illumination were employed. As depicted in Fig. 5a, the 4BFO/MSe material exhibited the highest current density, aligning with the superior photocatalytic H₂O₂ generation rate. Similarly, the 4BFO/MSe material displayed the smallest semicircle and the lowest interfacial charge-transfer resistance among all the samples in the EIS Nyquist plot (Fig. 5b). This observation indicated that the interface resistance decreased owing to the accumulation of photoelectrons at the interface between 1 T/2 H MoSe₂ and BFO material. Overall, these findings signified that the incorporation of 1 T/2 H MoSe₂ into BFO accelerated the transfer and separation of photogenerated charges.

Additionally, photocurrent-time curves and EIS were performed for a deeper comprehension of various phase MoSe₂ (Fig. S9). When comparing 2 H phase MoSe₂, it was evident that 1 T/2 H MoSe₂ exhibited significantly enhanced photo-response and superior charge carrier separation efficiency. Additionally, it demonstrated the lowest charge transfer resistance and higher electrical conductivity, as reflected by its smaller semicircle in the high-frequency region. These insights suggested that 1 T phase MoSe₂ may possess improved conductivity and

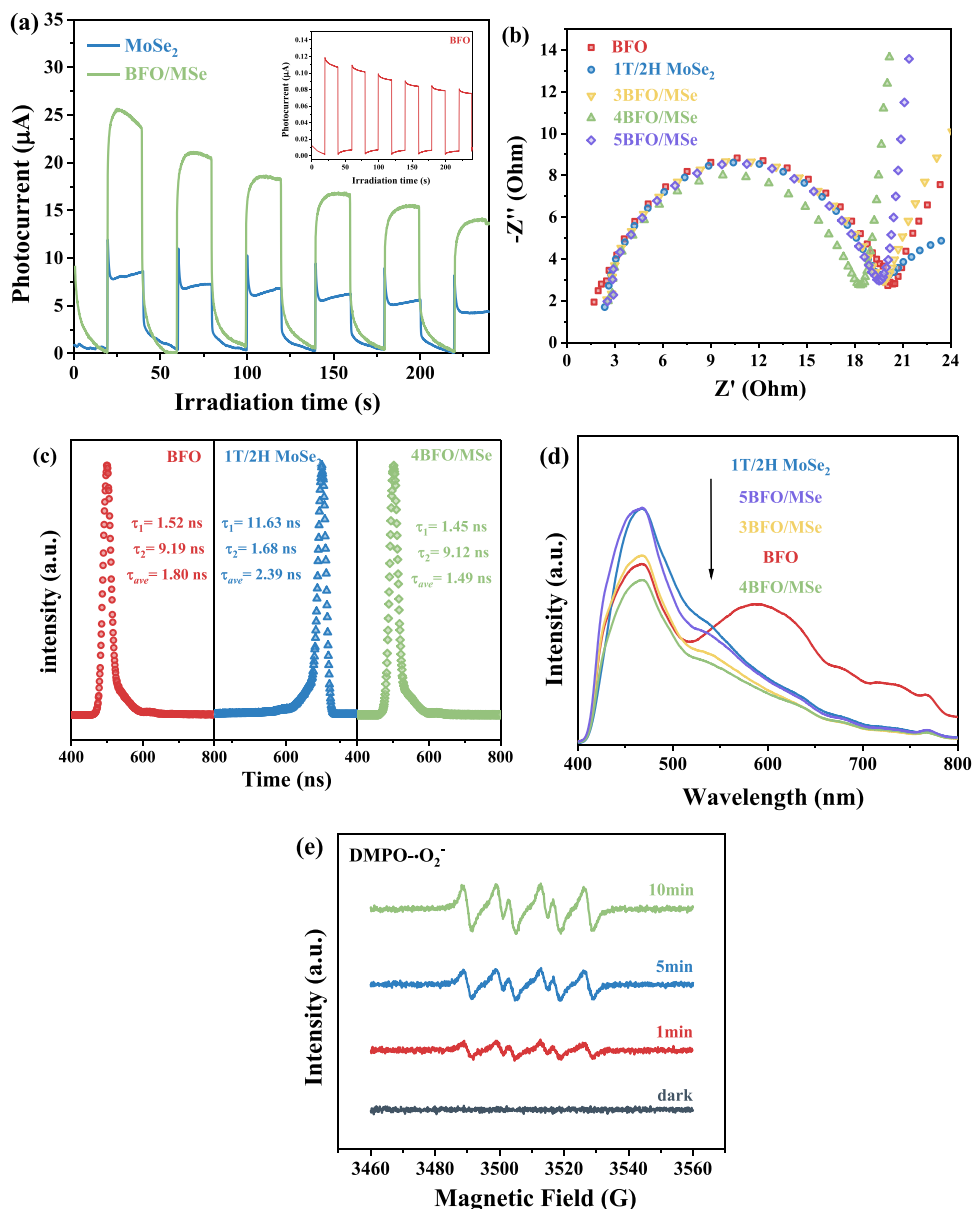


Fig. 5. (a) Transient photocurrent response of BFO, 1 T/2 H MoSe₂ and 4BFO/MSe; (b) Electrochemical impedance spectrum of BFO, 1 T/2 H MoSe₂ and BFO/MSe; (c) TRPL spectrum of BFO, 1 T/2 H MoSe₂ and 4BFO/MSe; (d) PL spectrum of BFO, 1 T/2 H MoSe₂ and BFO/MSe. EPR spectra of (e) DMPO-•O₂⁻ of 4BFO/MSe.

light sensitivity, with 1 T/2 H phase MoSe₂ exhibiting the most pronounced photoelectric activity.

TRPL and PL technologies were used to further analyze the separation efficiency and charge carrier transfer of samples. The TRPL spectra of BFO, 1 T/2 H MoSe₂, and BFO/MSe material were shown in Fig. 5c, which investigated the particular charge carrier dynamics of nano-systems [60,61]. A double exponential function was used to fit the fluorescence decay curve [62]. Furthermore, Table S3 showed the fitting parameters for BFO, 1 T/2 H MoSe₂, and BFO/MSe material. The τ_{ave} for BFO, 1 T/2 H MoSe₂, and 4BFO/MSe material, respectively, were 1.80, 2.39, and 1.49 ns. The lifetime of a singlet exciton was considerably reduced in the 4BFO/MSe photocatalyst, implying the formation of an electron transfer channel from BFO to 1 T/2 H MoSe₂. The PL spectroscopy supported the results presented. As illustrated in Fig. 5d, the PL intensity of 4BFO/MSe catalyst was observed to be the least, indicating that the integration of BFO and 1 T/2 H MoSe₂ suppressed the recombination of photogenerated carriers. This led to an augmentation in the quantity of efficient photogenerated electrons and holes, consequently elevating the photocatalytic efficiency of the composites.

To further identify the free radicals produced during photocatalysis, an EPR investigation was carried out. The EPR signals of $\bullet\text{O}_2$ for the 4BFO/MSe catalyst both revealed strong signals upon exposure to light, as shown in Fig. 5e. This was supported by the quenching experiment findings (Fig. S10). O₂ may play a significant role in the generation of photocatalytic H₂O₂ as evidenced by the fact that the H₂O₂ produced under air-equilibrated conditions was mostly quenched. Furthermore, AgNO₃ and p-benzoquinone (BQ) were commonly utilized as scavengers for e⁻ and $\bullet\text{O}_2$ species, respectively. Upon the addition of BQ and AgNO₃, the photocatalytic generation of H₂O₂ was significantly suppressed. In the absence of EG functioning as a scavenger for positive h⁺, minimal H₂O₂ was generated. Consequently, it can be inferred that both e⁻ and $\bullet\text{O}_2$ species predominantly participate in the reduction of O₂ to H₂O₂ through two consecutive one-electron processes (O₂ + e⁻ → $\bullet\text{O}_2$, $\bullet\text{O}_2$ + e⁻ + 2 H⁺ → H₂O₂).

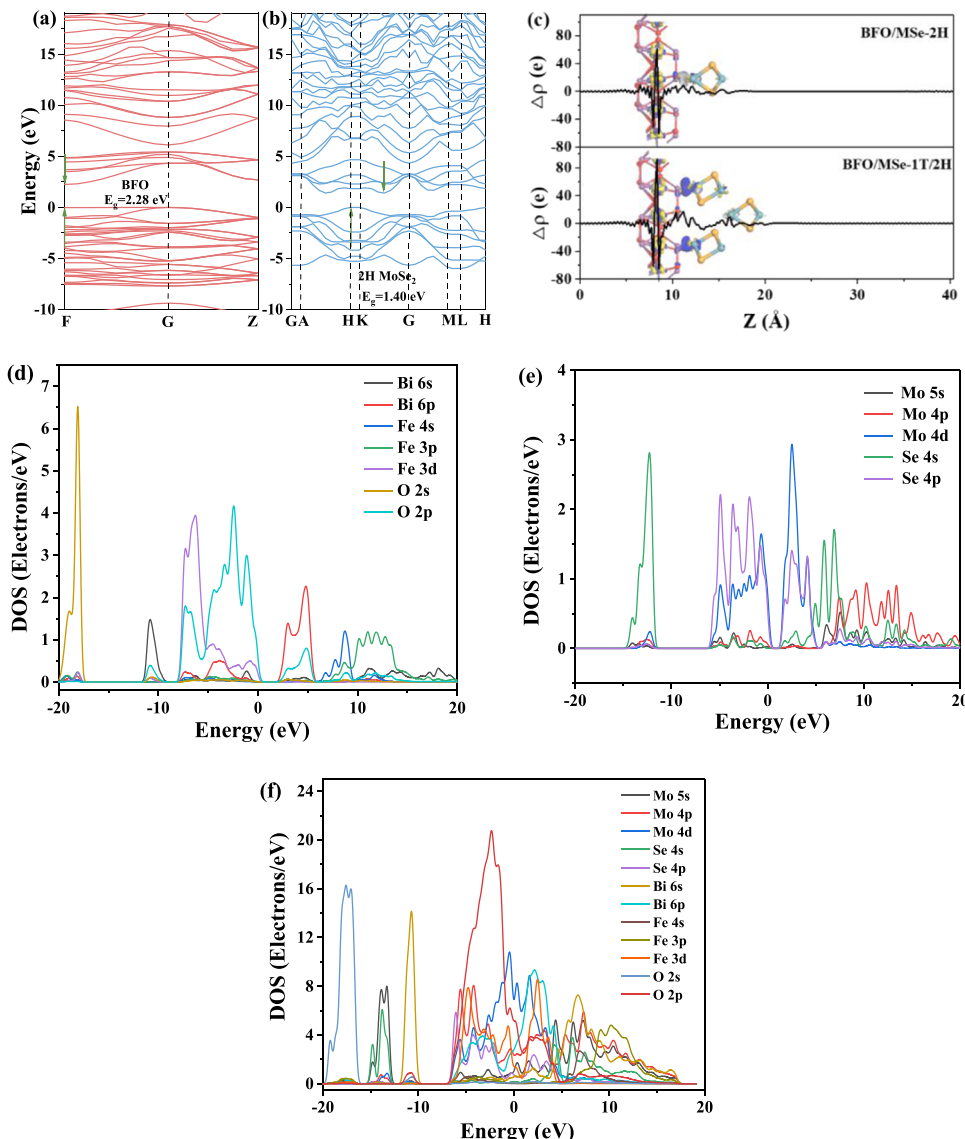


Fig. 6. Calculated electronic band structures of (a) BFO, (b) 2 H MoSe₂; (c) The profile of planar averaged charge density difference and three-dimensional charge density difference for the BFO/MSe-2 H and BFO/MSe-1 T/2 H heterojunctions (the color of blue and yellow mean the electrons and holes, respectively); Corresponding PDOS of (d) BFO, (e) 2 H MoSe₂ and (f) BFO/MSe.

3.5. Exploration of the synergistic mechanism

3.5.1. Investigation of electronic structure

The electronic structures were elucidated through DFT calculations (Fig. S11). These computations revealed that BFO manifested as a direct semiconductor, substantiated by the vertical misalignment between the CB minimum and VB maximum. In contrast, 2 H MoSe₂ displayed attributes of an indirect semiconductor, a characterization substantiated by the vertical alignment between the CB minimum and VB maximum, as illustrated in Fig. 6a and b [63]. In terms of computed bandgap energies (E_g), BFO and 2 H MoSe₂ were calculated to possess values of 2.28 and 1.40 eV, respectively [64]. It was worth noting that any disparities between these calculated values and the actual outcomes were attributed to the limitations of the exchange-correlation function in accurately describing excited states, as previously documented [65,66]. Furthermore, the Fermi level of 1 T MoSe₂ crossed across the CB (Fig. S12), demonstrating that the material was metallic and that electrons may rapidly gain energy and leap to the CB to conduct electricity. Following that, a heterojunction model based on BFO and MoSe₂ was created (Fig. S13). The calculated charge density difference distribution visibly confirmed the significant electronic connection between the BFO and MoSe₂ phases as shown in Fig. 6c. Charge accumulation and depletion in the FeO₄ units surrounding the interface of the BFO/MSe heterojunction were clearly visible. The Fe cation in the BFO appeared to have transferred electrons to the Mo cation in the MoSe₂ through the interfacial O atom. The enhanced charge density in the 1 T MoSe₂ structure demonstrated that the metal phase in the 1 T MoSe₂ structure had more effective charge transfer and active surface reaction sites. On the other hand, the computation of the partial densities of states (PDOS) of BFO, MoSe₂, and BFO/MSe catalyst (Fig. 6d-f) was used to examine the impact of interfacial charge transfer on the electronic structure. In the catalytic process, the charge was clearly transferred easily transferred from the Fe-d and O-p orbitals of the BFO to the Mo-d orbital of the MoSe₂. The theoretical Fermi level of the BFO may be shifted to a lower

position due to the loss of electrons, but the Fermi level of the MoSe₂ may be higher due to the gap state formed (Fig. S14). In conclusion, the coupling of iron and molybdenum had a significant part in the interfacial charge transfer that occurred between the units as a result of heterojunctions formation. As a result, the electrical architectures of the BFO and MoSe₂ in the BFO/MSe catalyst were modified.

3.5.2. Triggering Se sites

According to the above results and analysis, the electron transfer from BFO to 2 H MoSe₂ can greatly enhance the H₂O₂ production efficiency of BFO/MSe photocatalysts. To reveal the enhanced H₂O₂ generation mechanism, the introduction of BFO caused a modulation of the Mo-Se bond in 2 H MoSe₂, which was prioritized by DFT calculations. In order to identify the mutation of Mo-Se bonds caused by the introduction of BFO, the related electron localization function (ELF) of 2 H MoSe₂ and BFO/MSe-2 H catalyst was determined. The 2 H MoSe₂ structure exhibited a high charge density between Mo and Se atoms, demonstrating the strong binding force of the Mo-Se bond (Fig. 7a). After introducing BFO into the 2 H MoSe₂, the electron density of the Mo-Se bonds fell in BFO/MSe-2 H catalyst, suggesting their weaker occupancy state. The absence of an anti-bonding state below the E_f was evident in 2 H MoSe₂ was evident, whereas it was observed in the BFO/MSe-2 H catalyst. This observation confirmed that the incorporation of BFO weakened the Mo-Se binding strength (Fig. S15). Additionally, the diminished d-electron number (ε_d) may be used to confirm the weakened Mo-Se bonds. Specifically, the PDOS in Fig. 7b showed that the ε_d value of the Mo atoms was reduced from 0.42 (2 H MoSe₂) to -0.28 (BFO/MSe-2 H). The resulting PDOS data for Se (Fig. 7c) illustrated that the Mo-Se bonds, which were weakened due to the reduced number of d-orbital electrons, had a pronounced effect on diminishing the electron density surrounding Se atoms within the BFO/MSe structure. Notably, the in-plane Se site in the BFO/MSe-2 H structure exhibited a significantly lower electron occupancy compared to the Se site in 2 H MoSe₂. In contrast to 2 H MoSe₂, this reduction in electron occupancy distinctly

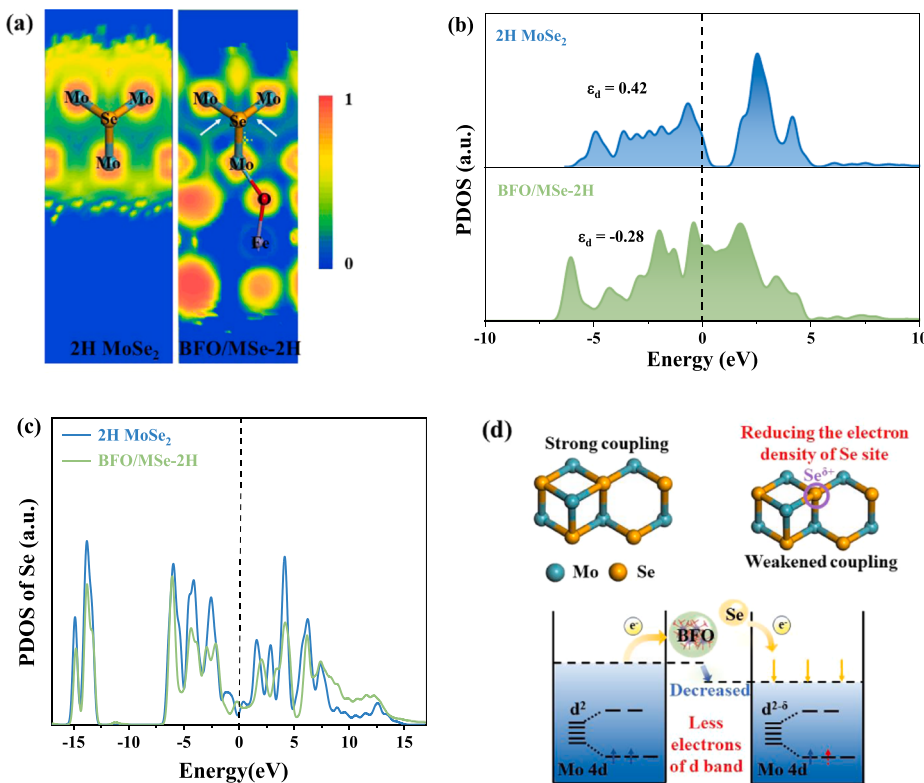


Fig. 7. (a) Corresponding electron localization function (ELF) patterns; (b) Density of states (DOS) plots of Mo-Se in 2 H MoSe₂ and BFO/MSe-2 H; (c) The PDOS results of Se sites in 2 H MoSe₂ and BFO/MSe-2 H; (d) Schematic illustration of the weakened coupling after BFO incorporation.

indicates a decrease in electron density at the Se sites, resulting in the formation of electron-deficient Se sites ($\text{Se}^{\delta+}$) within the BFO/MSe catalyst. Thus, it can be deduced that adding BFO material may effectively reduce the strength of the Mo-Se bond, resulting in the formation of $\text{Se}^{\delta+}$ in BFO/MSe catalysts for future H_2O_2 production (Fig. 7d). The adsorption capabilities of these Se sites towards O intermediates can be greatly influenced. As illustrated in Fig. S16, there was a notable correspondence between the 2p orbital of the active Se atoms and the 2p orbitals of O. This correspondence suggested a plausible capability for p-p orbital hybridization, implying that O could potentially adsorb onto Se atoms, forming $\text{Se}-\text{O}_{\text{ads}}$ bonds. Simultaneously, the O_2 desorption

temperature of BFO/MSe was fully displayed by O_2 -TPD (Fig. S17), demonstrating the strong O_2 adsorption ability of BFO/MSe. Then, the curve of BFO/MSe can be deconvoluted into two peaks: < 400 °C and 400–500 °C, corresponding to surface adsorbed oxygen (O_A) and surface lattice oxygen, respectively. In addition, the spectrum showed another characteristic peak at 94 °C, indicating the formation of new oxygen species on the surface, confirming O_2 activation. This was also confirmed by the XPS spectrum of O 1 s shown in Fig. S18a. The abundance of identifiable O_A in used BFO/MSe was higher than that in fresh BFO/MSe materials, indicating that used BFO/MSe (28.17 %) had a higher adsorbed oxygen concentration than fresh BFO/MSe (15.34 %).

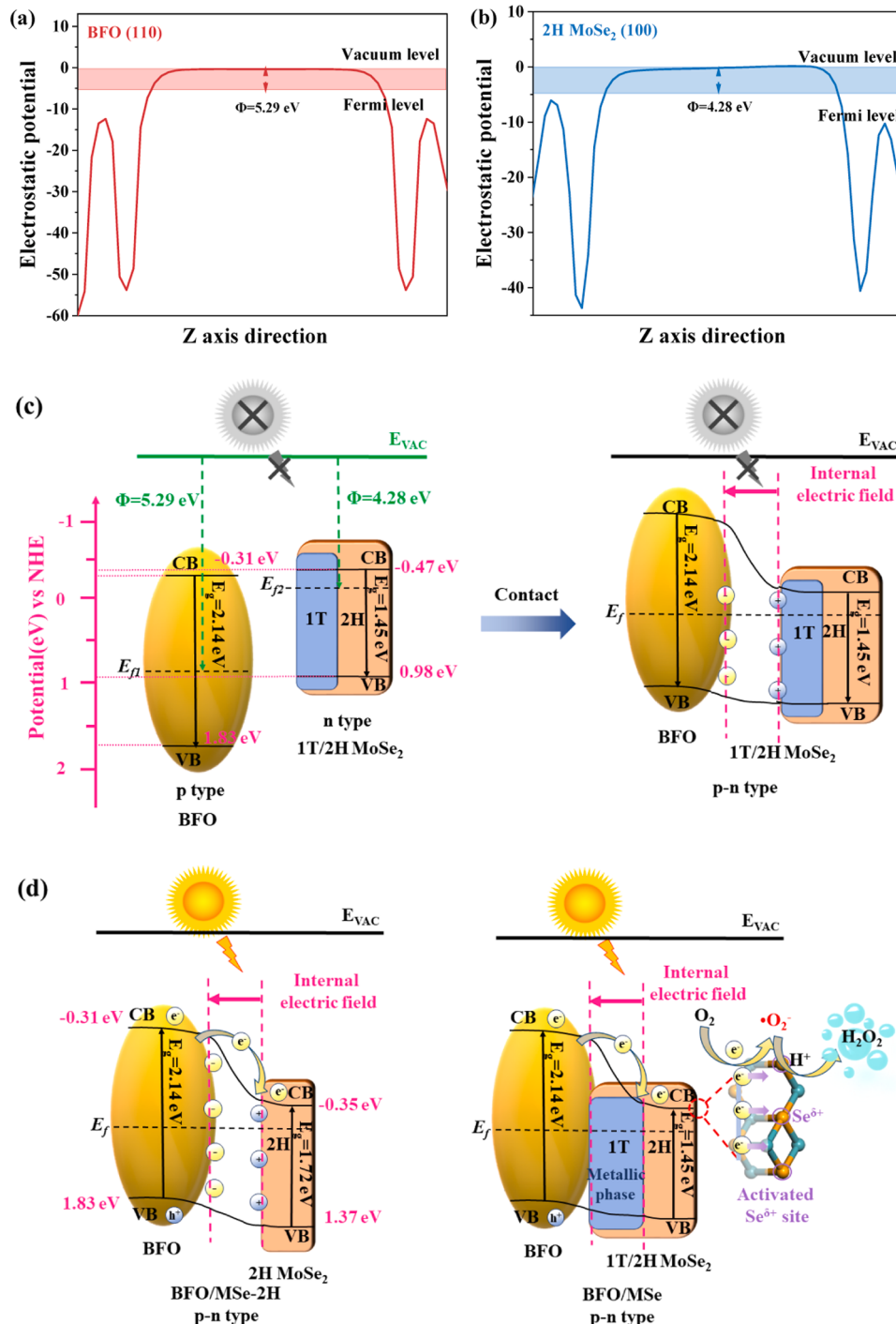


Fig. 8. Calculated average potential profile along the Z-axis of (a) BFO and (b) 2H MoSe₂; (c) Schematic diagram for the promoted photoelectron transfer under the enforcement of internal electric field; (d) Schematic illustration for the photocatalytic mechanism of BFO/MSe-2H and BFO/MSe under visible-light irradiation.

During the reaction process, BFO/MSe materials had an adsorption effect on O₂, which will greatly promote the catalytic reaction. The binding energy of the XPS spectrum of Se 3d at 58.7 eV represented the Se-O bond, which was attributed to a chemical reaction between O₂ (Fig. S18b). Therefore, the Se^{δ+} sites within the BFO/MSe catalysts accelerated the redox cycling of transition metals, thereby accelerating the production of reactive oxygen species.

3.5.3. The p-n type BFO/MSe heterojunctions mechanism

As depicted in Fig. 8a and b, the theoretical work functions (Φ) for the (110) surface of BFO and the (100) surface of 2 H MoSe₂ were computed to be 5.29 and 4.28 eV, respectively. Consequently, the Fermi levels for BFO and 2 H MoSe₂ were determined to be -5.29 and -4.28 eV vs. vacuum level [67,68]. Integrating the above results and analysis, the energy band configuration and the pathway of charge carrier migration can be elucidated in Fig. 8c. 2 H MoSe₂ exhibited a more negative E_f compared to BFO, indicating that the migration of electrons from 2 H MoSe₂ to BFO was energetically more favorable during the formation of a p-n type heterojunction between the two materials [69]. Upon achieving equilibrium, an electron depletion layer (representing a positive charge region) manifested near the interface of the 2 H MoSe₂ surface. In parallel, an electron accumulation layer (indicating a negative charge region) formed in the vicinity of the BFO surface near the interface. Additionally, the energy bands of the 2 H MoSe₂ underwent an upward bend due to electron loss, while the energy bands of the BFO exhibited a downward bend. Concurrently, the IEF between BFO and 2 H MoSe₂ was expected to facilitate a more rapid separation of strongly redox-capable electron-hole pairs.

Subsequently, the pivotal role played by the metallic phase of 1 T MoSe₂ introduced within the BFO/MSe heterostructure was elucidated, as depicted in Fig. 8d. The pathway for charge carrier transfer between 2 H MoSe₂ and BFO aligns with the p-n type II mechanism. The metallic-phase 1 T MoSe₂ acts as a bridge for charge carrier transfer between BFO and 2 H MoSe₂, significantly enhancing the transport of charges across the BFO/MSe heterojunction. Concurrently, the metallic-phase 1 T MoSe₂ catalyst effectively facilitates the separation of photoexcited charges in BFO, ensuring an ample supply of photogenerated electrons to participate in H₂O₂ production reactions at various activated Se sites within the interfacial region.

Overall, within the BFO/MSe heterojunctions, the presence of 1 T metallic-phase MoSe₂ facilitated the efficient separation of electron-hole pairs at the heterojunction interface. Photogenerated electrons triggered by visible light migrated smoothly from the CB of the p-type BFO to that of the n-type 1 T/2 H MoSe₂. Consequently, the polarization field established at their interface enhanced the disjunction of electrons and holes, maintaining their concentrations at a specific level and showcasing notable redox capabilities. Furthermore, the formation of an IEF induced a consequent bending of the energy bands of the p-n type BFO/MSe heterojunctions. This bending behavior endowed the CB edge with a more negative redox potential compared to O₂/•O₂. Consequently, electrons engaged with dissolved O₂ in water to generate •O₂ free radicals. Additionally, the formation of Se^{δ+} in BFO/MSe catalysts facilitates the adsorption and activation of O₂, effectively reducing the total activation energy barrier for O₂. Consequently, H₂O₂ is produced via a two-electron reduction process (O₂ + e⁻ → •O₂, •O₂ + e⁻ + 2 H⁺ → H₂O₂). The photoexcited h⁺ oxidizing EG alcohols to aldehydes and providing protons for H₂O₂ production. However, from Fig. S19, EPR revealed a small amount of •OH in BFO/MSe heterojunctions, which was attributed to the micro decomposition of H₂O₂. As shown in Fig. 3c, especially for 4BFO/MSe, showed an increase in the photon energy dependence of K_f while maintaining a low K_d, indicating high accumulation and low decomposition of H₂O₂. Subsequently, the stability of the BFO/MSe was demonstrated by long-term tests (Fig. S20) and ion leaching experiments (Fig. S21). After five cycles, the leaching concentrations of Mo and Fe were 71.525 μg·L⁻¹ and 104.13 μg·L⁻¹, respectively. And in ten cycles, the production of H₂O₂ from the 4BFO/MSe material was relatively

stable, indicating that a small amount of •OH and leached Mo and Fe did not contribute significantly to the reaction. Thus, the BFO/MSe catalyst exhibits enhanced photocatalytic activity in the synthesis of H₂O₂.

4. Conclusion

In conclusion, a novel and stable multiphasic catalyst composed of integrated 1 T/2 H MoSe₂ nanosheets with BFO was successfully synthesized to facilitate H₂O₂ production under visible light irradiation. The optimal 4BFO/MSe sample achieved an impressive production rate of 1640 μmol·g⁻¹·h⁻¹. The enhanced catalytic activity can be attributed to several factors: 1) the BFO/MSe catalyst exhibited superior light absorption capacity and enhanced charge separation efficiency compared to BFO and 1 T/2 H MoSe₂; 2) the 1 T/2 H MoSe₂ structure provided more active sites and a favorable band structure compared to 2 H MoSe₂; 3) the strong polarizing electric field generated by BFO and 1 T/2 H MoSe₂ accelerated carrier separation; 4) the integration of BFO into 1 T/2 H MoSe₂ optimized the electron density of Se sites, strengthening the Se-O_{ads} bond. This study not only clarified the pivotal role of bonding structures in finely modulating the electronic states of active sites but also introduced a novel perspective for the design of efficient catalysts for photocatalytic H₂O₂ production.

CRediT authorship contribution statement

Shen Junwei: Investigation, Validation. **Lu Bianhe:** Investigation, Validation. **Tang Sijing:** Investigation, Validation. **He Yuxuan:** Investigation, Visualization. **Liu Yin:** Investigation, Validation. **Qian Jin:** Conceptualization, Funding acquisition, Resources, Supervision, Writing – original draft, Writing – review & editing. **Xu Kailin:** Investigation, Visualization, Writing – original draft, Writing – review & editing. **Zhu Yueming:** Resources, Supervision, Writing – review & editing.

Declaration of Competing Interest

The authors declare that they have no known competing financial interests or personal relationships that could have appeared to influence the work reported in this paper.

Data availability

Data will be made available on request.

Acknowledgements

This study was financially supported by the National Key Plan for Research and Development of China (No. 2016YFC0401703), the National Natural Science Foundation of China (No. 51779078), the Six Talent Peaks Project in Jiangsu Province (No. JNHB-012), the National Major Projects of Water Pollution Control and Management Technology (No. 2017ZX07204003), and Priority Academic Program Development of Jiangsu Higher Education Institutions (PAPD).

Appendix A. Supporting information

Supplementary data associated with this article can be found in the online version at doi:10.1016/j.apcatb.2023.123571.

References

- [1] Y. Si, Y. Zhang, L. Lu, S. Zhang, Y. Chen, J. Liu, H. Jin, S. Hou, K. Dai, W. Song, Boosting visible light photocatalytic hydrogen evolution of graphitic carbon nitride via enhancing its interfacial redox activity with cobalt/nitrogen doped tubular graphitic carbon, *Appl. Catal. B Environ.* 225 (2018) 512–518.

- [2] J. Luo, X. Wei, Y. Qiao, C. Wu, L. Li, L. Chen, J. Shi, Photoredox-promoted co-production of dihydroisoquinoline and H₂O₂ over defective Zn₃In₂S₆, *Adv. Mater.* 35 (2023), 220110.
- [3] X. Deng, R. Chen, C. Wang, Z. Liang, Z. Zhao, W. Shi, F. Cui, Iron-tungsten oxides modified oxygen-rich carbon nitride with defects S-scheme heterojunction for boosting photo-Fenton like removal of pollutants, *Chem. Eng. J.* 451 (2023), 138629.
- [4] Y. Xia, X. Zhao, C. Xia, Z.Y. Wu, P. Zhu, J.Y. Kim, X. Bai, G. Gao, Y. Hu, J. Zhong, Y. Liu, H. Wang, Highly active and selective oxygen reduction to H₂O₂ on boron-doped carbon for high production rates, *Nat. Commun.* 12 (2021) 4225.
- [5] H. Xiong, D. Zou, D. Zhou, S. Dong, J. Wang, B.E. Rittmann, Enhancing degradation and mineralization of tetracycline using intimately coupled photocatalysis and biodegradation (ICPB), *Chem. Eng. J.* 316 (2017) 7–14.
- [6] S.A. Monny, Z. Wang, M. Konarova, L. Wang, Bismuth based photoelectrodes for solar water splitting, *J. Energy Chem.* 61 (2021) 517–530.
- [7] X. Huang, K. Wang, Y. Wang, B. Wang, L. Zhang, F. Gao, Y. Zhao, W. Feng, S. Zhang, P. Liu, Enhanced charge carrier separation to improve hydrogen production efficiency by ferroelectric spontaneous polarization electric field, *Appl. Catal. B Environ.* 227 (2018) 322–329.
- [8] Y. Zhang, L. Yang, Y. Zhang, Z. Ding, M. Wu, Y. Zhou, C. Diao, H. Zheng, X. Wang, Z.L. Wang, Enhanced photovoltaic performances of La-doped bismuth ferrite/zinc oxide heterojunction by coupling piezo-phototronic effect and ferroelectricity, *ACS Nano* 14 (2020) 10723–10732.
- [9] Y. Liu, S. Ye, H. Xie, J. Zhu, Q. Shi, N. Ta, R. Chen, Y. Gao, H. An, W. Nie, H. Jing, F. Fan, C. Li, Internal-field-enhanced charge separation in a single-domain ferroelectric PbTiO₃ photocatalyst, *Adv. Mater.* 32 (2020), 1906513.
- [10] Y. He, L. Zhang, X. An, G. Wan, W. Zhu, Y. Luo, Enhanced fluoride removal from water by rare earth (La and Ce) modified alumina: adsorption isotherms, kinetics, thermodynamics and mechanism, *Sci. Total Environ.* 688 (2019) 184–198.
- [11] K. Saravananakumar, C.M. Park, Rational design of a novel LaFeO₃/g-C₃N₄/BiFeO₃ double Z-scheme structure: photocatalytic performance for antibiotic degradation and mechanistic insight, *Chem. Eng. J.* 423 (2021), 130076.
- [12] M. Sun, C. Ma, M. Ma, Y. Wei, S. Dong, X. Zhang, J. Tian, M. Shao, Electrochemical ammonia synthesis via nitrogen reduction reaction on 1T/2H mixed-phase MoSe₂ catalyst: theoretical and experimental studies, *Mater. Today Phys.* 30 (2023), 100945.
- [13] A. Kumar, G. Sharma, Mu Naushad, T. Ahamed, R.C. Veses, F.J. Stadler, Highly visible active Ag₂CrO₄/Ag/BiFeO₃@RGO nano-junction for photoreduction of CO₂ and photocatalytic removal of ciprofloxacin and bromate ions: the triggering effect of Ag and RGO, *Chem. Eng. J.* 370 (2019) 148–165.
- [14] L. Zhao, J. Bian, X. Zhang, L. Bai, L. Xu, Y. Qu, Z. Li, Y. Li, L. Jing, Construction of ultrathin S-scheme heterojunctions of single Ni atom immobilized Ti-MOF and BiVO₄ for CO₂ photoconversion of nearly 100% to CO by pure water, *Adv. Mater.* 34 (2022), 2205303.
- [15] S. Batool, S.P. Nandan, S.N. Myakala, A. Rajagopal, J.S. Schubert, P. Ayala, S. Naghd, H. Saito, J. Bernardi, C. Streb, A. Cherevan, D. Eder, Surface anchoring and active sites of [Mo₅S₁₃]²⁻ clusters as co-catalysts for photocatalytic hydrogen evolution, *ACS Catal.* 12 (2022) 6641–6650.
- [16] Y. He, J. Qian, P. Wang, B. Lu, S. Tang, J. Li, Y. Liu, P. Gao, Modulating cobalt-iron electron transfer via encapsulated structure for enhanced catalytic activity in photo-peroxymonosulfate coupling system, *J. Hazard. Mater.* 439 (2022), 129609.
- [17] L. Zhang, J. Liang, L. Yue, Z. Xu, K. Dong, Q. Liu, Y. Luo, T. Li, X. Cheng, G. Cui, B. Tang, A.A. Alshehri, K.A. Alzahrani, X. Guo, X. Sun, N-doped carbon nanotubes supported CoSe₂ nanoparticles: a highly efficient and stable catalyst for H₂O₂ electroynthesis in acidic media, *Nano Res.* 15 (2022) 304–309.
- [18] H. Zhu, G. Gao, M. Du, J. Zhou, K. Wang, W. Wu, X. Chen, Y. Li, P. Ma, W. Dong, F. Duan, M. Chen, G. Wu, J. Wu, H. Yang, S. Guo, Atomic-scale core/shell structure engineering induces precise tensile strain to boost hydrogen evolution catalysis, *Adv. Mater.* 30 (2018), 1707301.
- [19] H. He, H. Zhang, D. Huang, W. Kuang, X. Li, J. Hao, Z. Guo, C. Zhang, Harnessing plasma-assisted doping engineering to stabilize metallic phase MoSe₂ for fast and durable sodium-ion storage, *Adv. Mater.* 34 (2022), 2200397.
- [20] S. Deng, F. Yang, Q. Zhang, Y. Zhong, Y. Zeng, S. Lin, X. Wang, X. Lu, C.Z. Wang, L. Gu, X. Xia, J. Tu, Phase modulation of (¹T-²H)-MoSe₂/TiC-C shell/core arrays via nitrogen doping for highly efficient hydrogen evolution reaction, *Adv. Mater.* 30 (2018), 1802223.
- [21] Y. Wang, X. Xiao, J. Chen, M. Lu, X. Zeng, 1T phase boosted MoSe₂/pg-C₃N₄ with Z-scheme heterojunction for enhanced photocatalytic degradation of contaminants, *Appl. Surf. Sci.* 510 (2020), 145341.
- [22] Z. Zhang, C. Jiang, P. Li, K. Yao, Z. Zhao, J. Fan, H. Li, H. Wang, Benchmarking phases of ruthenium dichalcogenides for electrocatalysis of hydrogen evolution: theoretical and experimental insights, *Small* 17 (2021), 2007333.
- [23] W. Zhong, B. Zhao, H. Yu, J. Fan, Simultaneously optimizing the number and efficiency of active Se sites in Se-rich a-MoSe_x nanodot cocatalysts for efficient photocatalytic H₂ evolution, *Sol. RRL* 6 (2022), 2100832.
- [24] Y.B. Kang, X. Han, S. Kim, H. Yuan, N. Ling, H.C. Ham, L. Dai, H.S. Park, Structural engineering of ultrathin ReS₂ on hierarchically architected graphene for enhanced oxygen reduction, *ACS Nano* 15 (2021) 5560–5566.
- [25] In situ cascade growth-induced strong coupling effect toward efficient photocatalytic hydrogen evolution of ReS₂/ZnIn₂S₄, *Appl. Catal. B Environ.*, 328 (2023) 122493.
- [26] F.L. Wang, Y. Li, N. Wang, L. Zhu, A. Jain, Y.G. Wang, F.G. Chen, Enhanced magnetic, ferroelectric and optical properties of Sr and Co co-doped BiFeO₃ powders, *J. Alloy. Compd.* 810 (2019), 151941.
- [27] L. Li, Y. Liu, S. Zhang, M. Liang, F. Li, Y. Yuan, Enhanced mineralization of bisphenol A by eco-friendly BiFeO₃-MnO₂ composite: performance, mechanism and toxicity assessment, *J. Hazard. Mater.* 399 (2020), 122883.
- [28] L. Zhou, R. Wu, Y. Jiang, Z. Li, S. Wei, Construction of heterogeneous 1T/2H MoSe₂ homojunction nanosheets with excellent broad-spectrum photocatalytic activity, *J. Mater. Sci.* 57 (2022) 14386–14397.
- [29] Y. Qu, H. Medina, S.W. Wang, Y.C. Wang, C.W. Chen, T.Y. Su, A. Manikandan, K. Wang, Y.C. Shih, J.W. Chang, H.C. Kuo, C.Y. Lee, S.Y. Lu, G. Shen, Z.M. Wang, Y. L. Chueh, Wafer scale phase-engineered 1T- and 2H-MoSe₂/Mo core-shell 3D-hierarchical nanostructures toward efficient electrocatalytic hydrogen evolution reaction, *Adv. Mater.* 28 (2016) 9831–9838.
- [30] J. Du, W. Xing, J. Yu, J. Feng, L. Tang, W. Tang, Synergistic effect of intercalation and EDLC electrosorption of 2D/3D interconnected architectures to boost capacitive deionization for water desalination via MoSe₂/mesoporous carbon hollow spheres, *Water Res.* 235 (2023), 119831.
- [31] W. Wang, P. Li, H. Zheng, Q. Liu, F. Lv, J. Wu, H. Wang, S. Guo, Ultrathin layered SnSe nanoplates for low voltage, high-rate, and long-life alkali-ion batteries, *Small* 13 (2017), 1702228.
- [32] S. Kazhugusalamoorthy, P. Jegatheesan, R. Mohandoss, N.V. Giridharan, B. Karthikeyan, R.J. Joseyphus, S. Dhanuskodi, Investigations on the properties of pure and rare earth modified bismuth ferrite ceramics, *J. Alloy. Compd.* 493 (2010) 569–572.
- [33] A. Mukherjee, S. Basu, L.A.W. Green, N.T.K. Thanh, M. Pal, Enhanced multiferroic properties of Y and Mn codoped multiferroic BiFeO₃ nanoparticles, *J. Mater. Sci.* 50 (2015) 1891–1900.
- [34] R. Sha, S. Badhulika, Few layered MoS₂ grown on pencil graphite: a unique single-step approach to fabricate economical, binder-free electrode for supercapacitor applications, *Nanotechnology* 30 (2019), 035402.
- [35] N. Vishnu, S. Badhulika, Single step synthesis of MoSe₂–MoO₃ heterostructure for highly sensitive amperometric detection of nitrite in water samples of industrial areas, *Electroanalysis* 31 (2019) 2410–2416.
- [36] Q. Feng, K. Duan, H. Xie, M. Xue, Y. Du, C. Wang, Electrocatalytic hydrogen evolution reaction of 2H MoSe₂ nanoflowers and 2H-MoSe₂/α-MoO₃ heterostucture, *Electrochim. Acta* 222 (2016) 499–504.
- [37] Y. Deng, Z. Liu, A. Wang, D. Sun, Y. Chen, L. Yang, J. Pang, H. Li, H. Li, H. Liu, W. Zhou, Oxygen-incorporated MoX (X: S, Se or P) nanosheets via universal and controlled electrochemical anodic activation for enhanced hydrogen evolution activity, *Nano Energy* 62 (2019) 338–347.
- [38] S. Kang, H. Khan, C. Lee, K. Kwon, C. Sunyong, Lee, Investigation of hydrophobic MoSe₂ grown at edge sites on TiO₂ nanofibers for photocatalytic CO₂ reduction, *Chem. Eng. J.* 420 (2021), 130496.
- [39] U. Gupta, B.S. Naidu, U. Maitra, A. Singh, S.N. Shirodkar, U.V. Waghmare, C.N. R. Rao, Characterization of few-layer 1T MoSe₂ and its superior performance in the visible-light induced hydrogen evolution reaction, *APL Mater.* 2 (2014), 092802.
- [40] Y. Wang, Y. Tang, J. Sun, X. Wu, H. Liang, Y. Qu, L. Jing, BiFeO₃/Bi₂Fe₄O₉ S-scheme heterojunction hollow nanospheres for high-efficiency photocatalytic o-chlorophenol degradation, *Appl. Catal. B Environ.* 319 (2022), 121893.
- [41] T. Zhang, Z. Li, J. Zhong, J. Li, X. Tang, Photocatalytic properties of N-doped Bi₀/BiOI with abundant OV's for efficient detoxification of hazardous contaminants from environment, *Surf. Interfaces* 31 (2022), 102051.
- [42] L. Pei, X. Gu, Y. Zhang, J. Wang, H. Tan, P. Wang, Z. Zheng, Construction of nano-TiO₂ decorated titanosilicate core-shell structure: highly efficient oxygen activation for the degradation of Rhodamine B under visible light and excellent recycling performance, *J. Environ. Chem. Eng.* 9 (2021), 105815.
- [43] Y. Qi, S. Yuan, L. Cui, Z. Wang, X. He, W. Zhang, T. Asefa, (Fe,Co)/N-doped multi-walled carbon nanotubes as efficient bifunctional electrocatalysts for rechargeable zinc-air batteries, *ChemCatChem* 13 (2021) 1023–1033.
- [44] W. Fan, Z. Sun, Y. Bai, K. Wu, Y. Cheng, Highly stable and efficient perovskite ferrite electrode for symmetrical solid oxide fuel cells, *ACS Appl. Mater. Interfaces* 11 (2019) 23168–23179.
- [45] W.C. Huo, X. Dong, J.Y. Li, M. Liu, X.Y. Liu, Y.X. Zhang, F. Dong, Synthesis of Bi₂WO₆ with gradient oxygen vacancies for highly photocatalytic NO oxidation and mechanism study, *Chem. Eng. J.* 361 (2019) 129–138.
- [46] J. Wang, H. Guo, Y. Liu, W. Li, B. Yang, Peroxymonosulfate activation by porous BiFeO₃ for the degradation of bisphenol AF: non-radical and radical mechanism, *Appl. Surf. Sci.* 507 (2020), 145097.
- [47] N. Li, J. Wu, Y. Lu, Z. Zhao, H. Zhang, X. Li, Y.Z. Zheng, X. Tao, Stable multiphasic 1T/2H MoSe₂ nanosheets integrated with 1D sulfide semiconductor for drastically enhanced visible-light photocatalytic hydrogen evolution, *Appl. Catal. B Environ.* 238 (2018) 27–37.
- [48] X. Hu, W. Zhang, X. Liu, Y. Mei, Y. Huang, Nanostructured Mo-based electrode materials for electrochemical energy storage, *Chem. Soc. Rev.* 44 (2015) 2376–2404.
- [49] D. Pierucci, H. Henck, J. Avila, A. Balan, C.H. Naylor, G. Patriarche, Y.J. Dappe, M. G. Silly, F. Sirotti, A.T.C. Johnson, M.C. Asensio, A. Ouerghi, Band alignment and minigaps in monolayer MoS₂-graphene Van der Waals heterostructures, *Nano Lett.* 16 (2016) 4054–4061.
- [50] J. Ran, W. Guo, H. Wang, B. Zhu, J. Yu, S.Z. Qiao, Metal-free 2D/2D phosphorene/g-C₃N₄ Van der Waals heterojunction for highly enhanced visible-light photocatalytic H₂ production, *Adv. Mater.* 30 (2018) 1800128.
- [51] B. Liu, C. Bie, Y. Zhang, L. Wang, Y. Li, J. Yu, Hierarchically porous ZnO/g-C₃N₄ S-scheme heterojunction photocatalyst for efficient H₂O₂ production, *Langmuir* 37 (2021) 14114–14124.
- [52] S. Zhao, X. Zhao, Insights into the role of singlet oxygen in the photocatalytic hydrogen peroxide production over polyoxometalates-derived metal oxides

- incorporated into graphitic carbon nitride framework, *Appl. Catal. B Environ.* 250 (2019) 408–418.
- [53] Y. Yang, B. Cheng, J. Yu, L. Wang, W. Ho, $\text{TiO}_2/\text{In}_2\text{S}_3$ S-scheme photocatalyst with enhanced H_2O_2 -production activity, *Nano Res.* 16 (2023) 4506–4514.
- [54] J. Xu, Q. Zhang, X. Gao, P. Wang, H. Che, C. Tang, Y. Ao, Highly efficient feiⁱⁱ-initiated self-cycled Fenton system in Piezo-catalytic process for organic pollutants degradation, *Angew. Chem. Int. Ed.* 62 (2023), e202307018.
- [55] C. Dong, Y. Yang, X. Hu, Y. Cho, G. Jang, Y. Ao, L. Wang, J. Shen, J.H. Park, K. Zhang, Self-cycled photo-Fenton-like system based on an artificial leaf with a solar-to- H_2O_2 conversion efficiency of 1.46%, *Nat. Commun.* 13 (2022) 4982.
- [56] W. Liu, P. Wang, J. Chen, X. Gao, HuinanN. Che, B. Liu, Y. Ao, Unraveling the mechanism on ultrahigh efficiency photocatalytic H_2O_2 generation for dual-heteroatom incorporated polymeric carbon nitride, *Adv. Funct. Mater.* 32 (2022), 2205119.
- [57] P. Liu, Y. Liu, W. Ye, J. Ma, D. Gao, Flower-like N-doped MoS_2 for photocatalytic degradation of RhB by visible light irradiation, *Nanotechnology* 27 (2016), 225403.
- [58] C. Feng, Q. Gu, J. Rong, Q. Liang, M. Zhou, X. Li, S. Xu, Z. Li, Porous dual Z-scheme $\text{InOOH}/\text{RCN}/\text{CoWO}_4$ heterojunction with enhanced photothermal-photocatalytic properties towards norfloxacin degradation, *Sep. Purif. Technol.* 308 (2023), 122890.
- [59] L. Wang, J. Zhang, H. Yu, I.H. Patir, Y. Li, S. Wageh, A.A. Al-Ghamdi, J. Yu, Dynamics of photogenerated charge carriers in inorganic/organic S-scheme heterojunctions, *J. Phys. Chem. Lett.* 13 (2022) 4695–4700.
- [60] Z. Zhang, Y. Huang, K. Liu, L. Guo, Q. Yuan, B. Dong, Multichannel-improved charge-carrier dynamics in well-designed hetero-nanostructural plasmonic photocatalysts toward highly efficient solar-to-fuels conversion, *Adv. Mater.* 27 (2015) 5906–5914.
- [61] N. Zhang, M.Q. Yang, Z.R. Tang, Y.J. Xu, Toward improving the graphene–semiconductor composite photoactivity via the addition of metal ions as generic interfacial mediator, *ACS Nano* 8 (2014) 623–633.
- [62] Y. Yang, C. Zhang, D. Huang, G. Zeng, J. Huang, C. Lai, C. Zhou, W. Wang, H. Guo, W. Xue, R. Deng, M. Cheng, W. Xiong, Boron nitride quantum dots decorated ultrathin porous g-C₃N₄: intensified exciton dissociation and charge transfer for promoting visible-light-driven molecular oxygen activation, *Appl. Catal. B Environ.* 245 (2019) 87–99.
- [63] W.M.A. El Rouby, Selective adsorption and degradation of organic pollutants over Au decorated Co doped titanate nanotubes under simulated solar light irradiation, *J. Taiwan Inst. Chem. Eng.* 88 (2018) 201–214.
- [64] Y. Bian, W. Zeng, M. He, Y. Ma, Y. Liu, Y. Kong, J. Pan, Boosting charge transfer via molybdenum doping and electric-field effect in bismuth tungstate: density function theory calculation and potential applications, *J. Colloid Interface Sci.* 534 (2019) 20–30.
- [65] Y. Guo, C. Li, Z. Gong, Y. Guo, X. Wang, B. Gao, W. Qin, G. Wang, Photocatalytic decontamination of tetracycline and Cr(VI) by a novel α -FeOOH/FeS₂ photocatalyst: one-pot hydrothermal synthesis and Z-scheme reaction mechanism insight, *J. Hazard. Mater.* 397 (2020), 122580.
- [66] M. Pazoki, M.B. Johansson, H. Zhu, P. Broqvist, T. Edvinsson, G. Boschloo, E.M. J. Johansson, Bismuth iodide perovskite materials for solar cell applications: electronic structure, optical transitions, and directional charge transport, *J. Phys. Chem. C* 120 (2016) 29039–29046.
- [67] L. Kang, Z. Han, H. Yu, Q. Wu, H. Yang, Experimental and theoretical investigations on the enhanced photocatalytic performance of titanate nanosheets/sulfur-doped g-C₃N₄ heterojunction: synergistic effects and mechanistic studies, *Sep. Purif. Technol.* 278 (2021), 119482.
- [68] H. Ren, F. Qi, A. Labidi, J. Zhao, H. Wang, Y. Xin, J. Luo, C. Wang, Chemically bonded carbon quantum dots/ Bi_2WO_6 S-scheme heterojunction for boosted photocatalytic antibiotic degradation: interfacial engineering and mechanism insight, *Appl. Catal. B Environ.* 330 (2023), 122587.
- [69] Q. Zhou, L. Zhang, L. Zhang, B. Jiang, Y. Sun, In-situ constructed 2D/2D $\text{ZnIn}_2\text{S}_4/\text{Bi}_4\text{Ti}_3\text{O}_{12}$ S-scheme heterojunction for degradation of tetracycline: performance and mechanism insights, *J. Hazard. Mater.* 438 (2022), 129438.